Iterative passive-source location estimation and velocity inversion using geometric-mean reverse-time migration and full-waveform inversion

Bin Lyu[1] and Nori Nakata[2]

[1]*School of Geosciences, The University of Oklahoma, Norman, OK 73019, USA. E-mail: bin.lyu@ou.edu*
[2]*Earth, Atmospheric and Planetary Sciences, Massachusetts Institute of Technology, Cambridge, MA 02139, USA*

SUMMARY

Passive-seismic provides useful information for reservoir monitoring and structural imaging; for example, the locations of microseismic events are helpful to understand the extension of the hydraulic fracturing. However, passive-seismic imaging still faces some challenges. First, it is not easy to know where the passive-seismic events happened, which is known as passive-source locating. Additionally, the accuracy of the subsurface velocity model will influence the accuracy of the estimated passive-source locations and the quality of the structural imaging obtained from the passive-seismic data. Therefore the velocity inversion using the passive-seismic data is required to provide the velocity with higher accuracy. Focusing on these challenges, we develop an iterative passive-source location estimation and velocity inversion method using geometric-mean reverse-time migration (GmRTM) and full-waveform inversion (FWI). In each iteration, the source location is estimated using a high-resolution GmRTM method, which provides a better focusing of passive-source imaging compared to conventional wavefield scanning method. The passive-source FWI is then followed to optimize the velocity model using the estimated source location provided by GmRTM. The source location estimation and velocity inversion are implemented sequentially. We evaluate this iterative method using the Marmousi model data set. The experiment result and sensitivity analysis indicate that the proposed method is effective to locate the sources and optimize velocity model in the areas with complicated subsurface structures and noisy recordings.

Key words: Numerical modelling; Numerical solutions; Waveform inversion; Wave propagation.

1 INTRODUCTION

The subsurface reservoir properties could be identified using both the active and/or passive-seismic methods. A proven application of the passive-seismic method for oil and gas exploration is the microseismic due to hydraulic fracturing (e.g. Maxwell 2014; Witten & Shragge 2017). We generally use fracturing to extract the oil and gas from the subsurface rocks with low permeability such as shale (Maxwell 2014). To make the oil and gas flow more freely, a high-pressure liquid is then injected into the well to create fracture openings, which will result in microseismic events. We can use the locations of these seismic events to help understand the hydraulic fracturing. Locating microseismic events has also been used in understanding reservoir depletion (e.g. Dohmen *et al.* 2014) and monitoring seismically active faults (e.g. Wessels *et al.* 2011). Additionally, passive seismic provides useful information for subsurface structural imaging. For example, Dueker & Sheehan (1997) used a common conversion point (CCP) stacking technique to image the

interfaces in the crust and mantle. Shang *et al.* (2012) decoupled the multicomponent recorded data and then extrapolated the *P*- and *S*-wavefields for passive-source imaging.

However, we still face several challenges in the passive-seismic. The first one is how to accurately locate these passive-seismic events, which is known as passive-seismic source imaging. We can use the arrival-time differences between pairs of the events to estimate the passive-source-location, which is known as double-difference technique (Waldhauser & Ellsworth 2000). Later, waveform information is used for source-location estimation (Kao & Shan 2004), instead of simple the arrival times. Receiver wavefields are extrapolated in the reverse-time direction (McMechan 1982; Rietbrock & Scherbaum 1994; Gajewski & Tessmer 2005; Steiner *et al.* 2008; Duncan & Eisner 2010; Li *et al.* 2019, 2020), which generate a 4-D wavefield volume. Then scanning or threshold methods are used to find the focusing and estimate the source location. *P* and *S* waves could be simultaneously extrapolated using this time-reverse wave propagation method to locate passive

sources (e.g. Artman *et al.* 2010; Yang & Zhu 2019). Zhu (2014) further improved the imaging quality by compensating for attenuation. To collapse the time axis and improve the resolution of the passive-source imaging, Sun *et al.* (2015) and Nakata & Beroza (2015, 2016) developed a geometric-mean reverse-time migration (GmRTM) method, which is implemented by a zero-lag cross-correlation among all the independently back-propagated receiver wavefields.

Further, the precision of the subsurface velocity model is a key factor which will affect the estimation of the passive-source location. A velocity model with high precision and resolution is expected for the passive-seismic source imaging. The velocity model is also critical for the seismic structural imaging. Traveltime tomography (Aki *et al.* 1977; Pratt & Chapman 1992; Williamson & Worthington 1993) is commonly employed to estimate the subsurface velocity model but usually provides results with low resolution due to the limitation of the ray theory, which is based on the high-frequency assumption. To improve the resolution, wave equation-based velocity inversion approaches have been developed, which involve FWI, not only the traveltime. FWI (Tarantola 1984) provides a powerful tool to estimate the subsurface model with much higher spatial resolution over the traveltime tomography. FWI represents a series of methods to search for a model which best fits the observed waveforms (e.g. Virieux & Operto 2009).

FWI has been used in both active-seismic data (Virieux & Operto 2009; Xu *et al.* 2012; Warner *et al.* 2013) and passive-seismic data (Kamei & Lumley 2014, 2017; Zhu *et al.* 2015). For the active-seismic FWI, we usually know the source-locations and only need to estimate their signatures. But for the passive-seismic FWI, the unknown source information makes the FWI more challenging. A natural approach of passive FWI is to update the velocity model and source parameters simultaneously (Sun *et al.* 2016; Igonin & Innanen 2018; Wang & Alkhalifah 2018). However, the cross-talk between the velocity model and the source properties challenges the inversion, which is a common difficulty in all multiparameter FWI algorithms (Brossier *et al.* 2010; Operto *et al.* 2013; Innanen 2014; Pan *et al.* 2016; Wang *et al.* 2016).

In this paper, we develop an iterative passive-source estimation and velocity inversion method using GmRTM and FWI. In each iteration, we first estimate the source location using the high-resolution GmRTM method, which provides a better focusing of passive-source imaging compared to conventional wavefield scanning method. Next, the passive-source FWI is followed to optimize the velocity model using the estimated source location provided by GmRTM. The iterations are repeated until convergence, providing the optimized source imaging and velocity model. In this proposed method, the source location estimation and velocity inversion are implemented sequentially, which could partly relax the cross-talk limitation in the simultaneous FWI inversion.

This paper is organized as follows. We begin with this introduction. Next, we illustrate the detailed theory and method of the iterative passive-source estimation and velocity inversion. We then show the numerical results of the Marmousi model. Finally, we provide discussions and conclusions.

2 METHODOLOGY

Focusing on the above three challenges in passive-seismic, we develop an iterative passive-source estimation and velocity inversion method using GmRTM and FWI, which is shown in Fig. 1. We

first input the observed passive-seismic data, and the initial background velocity model, which could be provided by the ray-based tomography methods.

Next, we optimize the passive-source locations and velocity model in an iterative way. In each iteration, we first numerically propagate all the independent receiver or receiver-group wavefields in the reverse-time direction, followed by a zero-lag cross-correlation among all these wavefields, to provide passive-source imaging. This method is known as GmRTM, which provides passive-seismic source estimation with better focusing over conventional time-reversal imaging (Nakata & Beroza 2016). Further, we perform a passive-source FWI with these estimated source locations, to optimize the velocity model. In the next iteration, we repeat these two sequential steps using the optimized source locations and velocity model from previous iteration until convergence.

In this paper, we focus on this iterative approach of passive-source estimation and velocity inversion. Additionally, we can provide subsurface structural imaging using the optimized source locations and velocity model (see the Appendix). It is implemented by passive-source RTM using both the source- and receiver-side wavefields with a squared excitation-amplitude imaging condition. GmRTM and passive-source FWI are the key techniques used in the proposed iterative passive-source estimation and velocity inversion method.

2.1 Passive-source imaging using GmRTM

We start with the wave equation in isotropic acoustic media from a point source with location $\mathbf{x}_s$:

$$\left[\frac{1}{v^2(\mathbf{x})} \frac{\partial^2}{\partial t^2} - \nabla^2 \right] u(t, \mathbf{x}) = f(t) \delta(\mathbf{x} - \mathbf{x}_s), \qquad (1)$$

where $v(\mathbf{x})$ represents the medium velocity, $u(t, \mathbf{x})$ is the wavefield at time t and location $\mathbf{x}=(x, y, z)$, ∇^2 represents the Laplacian operator, and $f(t)$ is the wavelet function.

In eq. (1), $u(t, \mathbf{x})$ could represent both the forward-propagated wavefield $u_s(t, \mathbf{x})$ and the backward-propagated wavefield $u_r(t, \mathbf{x})$. For the time-reverse wave propagation method (e.g. Steiner *et al.* 2008), if the onset time is known, a passive source could be represented by the focusing of all backward-propagated events at the origin time. However, the time information is usually not available. We generally perform a scanning on the 4-D receiver wavefields $u_r(t, \mathbf{x})$, to find the time when the wavefields show the maximum amplitude and provide a focused image.

If we consider each receiver or receiver group independently, we can perform a cross-correlation between two or more receiver wavefields, for example the ones with different time lags, to provide another imaging condition. Because the recordings at these receivers are generated by the same seismic source, their corresponding wavefields pass the source location at the same time. We only need to consider the situation when the time lag equals zero (Claerbout 1971), which provides a new imaging condition known as GmRTM (Nakata & Beroza 2016),

$$\Im(\mathbf{x}) = \sum_t \prod_i u_{r_i}(t, \mathbf{x}). \qquad (2)$$

In GmRTM, we first extrapolate the wavefields at the desired receivers, to generate a 4-D data volume $u_{r_i}(t, \mathbf{x})$. Next, we multiply all these independent receiver wavefields at the whole space and time, and then sum them over the time axis, which is equivalent to the zero-lag cross-correlation. We can note that the time axis is
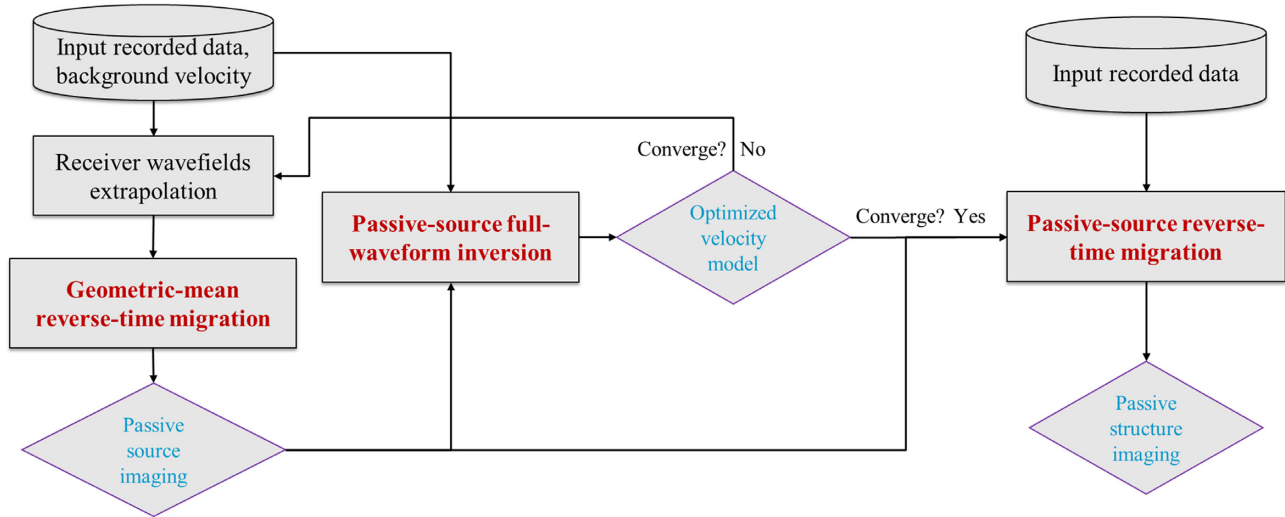
Figure 1. Iterative passive-source estimation and velocity inversion method using GmRTM and passive-source FWI.

collapsed in eq. (2) after the summation, which means that GmRTM reduces the dimensions of wavefields scanning method from 4-D to 3-D. The multiplication in GmRTM will produce images with non-zeros only at the focuses, while in the wavefields scanning method the summation over all the receiver wavefields will lead to images with non-zeros along the wave propagation path. This explains why the GmRTM provides source imaging results with higher spatial resolution.

To compute $u_{r_i}(t, \mathbf{x})$ in eq. (2), we need to perform wavefield extrapolation independently for each receiver or receiver group, which could be computationally expensive. A practical solution is to use the same Green's function for different time steps at each receiver (Nakata *et al.* 2016), to reduce the computational cost, which is due to the linear relationship between the Green's function and the recorded data. This idea is based on the fact that the length of our continuous seismic data is often days to years. This is much longer than the wave propagation time from the source to the receiver, which is typically in seconds. If we directly apply numerical wavefield extrapolation to the continuous data, we need to compute extrapolation for the entire data. Instead, Nakata *et al.* (2016) proposed that we first calculate the Green's function for each receiver, and then convolute between this Green's function and the recorded data in the image domain. Although we need to store each Green's function, the computational cost is much smaller than extrapolation of the entire records.

Since we do summation over the time axis as a part of cross-correlation, the source onset time is not a problem in GmRTM. If we are interested in that time, we can find it by selecting the summing time carefully. The source function is another important parameter and varies for different events. In this study, we used a known Ricker wavelet as the source function. We focus on estimating the source location in this paper. Similar to active-source cases (Pratt 1999), we can invert the source wavelet as well by updating the proposed method.

2.2 Velocity optimization using passive-source FWI

FWI uses a non-linear data-fitting procedure to provide detailed estimation of subsurface properties. Here, we primarily focus on the subsurface velocity variations. The general steps of FWI started

from an initial velocity model, which could be obtained using a ray-based tomography method. We compute predicted data from this initial model by solving the wave equation. We then update the velocity model, in order to decrease the misfit between the predicted data and the observed data. This optimization procedure is repeated in an iterative way, until the misfit is small enough to meet this criterion.

For passive-source FWI, the source-location is required to perform forward modeling, which is more challenging than active-seismic data. We optimize the passive-source locations and velocity model in an iterative way. In one iteration, an initial estimation of the source location $\mathbf{x}_{s0}$ is provided by the GmRTM using eq. (2), which is used to implement forward modeling using eq. (1), to generate the predicted data. The objective function is defined as the data misfit between the predicted data $\mathbf{d}_{pre}$ and the observed data $\mathbf{d}_{obs}$ at each receiver location $\mathbf{x}_g$ measured by the L_2 norm:

$$J = \sum_{\mathbf{x}_s} \sum_{\mathbf{x}_g} \frac{1}{2} \int \left[\mathbf{d}_{obs}\left(\mathbf{x}_{s0}, \mathbf{x}_g, t\right) - \mathbf{d}_{pre}\left(\mathbf{x}_{s0}, \mathbf{x}_g, t\right) \right]^2 dt. \quad (3)$$

To solve the above non-linear problem, local optimization methods are usually preferred due to their computational efficiency. The computation of the gradient with respect to the velocity model is important for FWI. Using the adjoint-state method (Plessix 2006), we calculate the gradient through the zero-lag cross-correlation between the forward-propagated source wavefields and the backward-propagated wavefields of the data residuals,

$$g(\mathbf{x}) = \frac{2}{v_0^3(\mathbf{x})} \sum_s \int \frac{\partial u_f(\mathbf{x}, t \,|\mathbf{x}_{s0})}{\partial t} \frac{\partial \delta u_f(\mathbf{x}, t \,|\mathbf{x}_{s0})}{\partial t} dt, \quad (4)$$

where $v_0(\mathbf{x})$ is the velocity model to be updated, $u_f(\mathbf{x}, t|\mathbf{x}_{s0})$ denotes the forward-propagated wavefield, and $\delta u_f(\mathbf{x}, t|\mathbf{x}_{s0})$ represents the backward-propagated wavefields of the data residuals.

After calculating the gradient with eq. (4), we use the conjugate gradient (CG) method (Mora 1987; Tarantola 1987) to update the velocity model. The step length is estimated by a line-search optimization scheme in each iteration. In the next iteration, we repeat GmRTM and passive-source FWI using the optimized source

locations and velocity model from the previous iteration until convergence.

3 NUMERICAL EXPERIMENTS

3.1 Experiment setup

We perform a numerical test on the Marmousi model to indicate the effectiveness of the full wave equation workflow for the passive-seismic imaging and velocity inversion. The true velocity model is shown in Fig. 2(a), with 576 lateral and 188 vertical samples both at 16 m cell size. However, the receivers are usually sparse in microseismic monitoring. In our experiment, the receivers are placed sparsely on the surface with 100 m interval.

The initial velocity model is shown in Fig. 2(b), which is seriously smoothed and relatively far from the true velocity model (Fig. 2a). This initial velocity model could be generated using a ray-based tomography method. We start with one source located at lateral position of 2.00 km and depth of 2.27 km (black dot in Fig. 2b). A 2-D acoustic finite-difference (FD) modeling method (e.g. McMechan 1983) is used to generate the synthetic recording.

3.2 Source location estimation and velocity inversion with single source

Using the initial velocity model (Fig. 2b), we first implement GmRTM using five receivers to estimate the source location. The enlarged display of GmRTM result is shown in Fig. 3, which has no time axis. We only need to scan the space axis to find the source location. The source location estimation is provided by finding the focusing in the imaging result (Fig. 3). However, there is an obvious deviation between the focusing and the true source location (red dot in Fig. 3) due to the velocity errors. The best focusing is found at the lateral location 1.93 km and depth 2.21 km. It is also noted that the focusing is poor, which also challenges the source location estimation.

Next, we perform passive-source FWI on the recording of the single source in an iterative way, to optimize the initial velocity model (Fig. 2b). The forward modeling in FWI is implemented using eq. (1), starting from the estimated source location (Fig. 3) using the initial velocity model (Fig. 2b). The predicted recording using the initial velocity model is shown in Fig. 4(b), which is far away from the observed recording (Fig. 4a). In Fig. 4(c), we show the predicted data using the FWI-inverted velocity model after 50 iterations, which reveals most of the details in the observed recording (Fig. 4a).

Fig. 5 shows the normalized misfit function versus iteration numbers. Fast convergence rate is observed in the first 17 iterations, and then the convergence becomes slower in the remaining iterations. The inverted velocity model after 50 iterations is shown in Fig. 6. The source location is indicated by the black dot. The source imprints are observed especially around the source. At present, we are using a smoothing method to reduce this source imprint artifact. More advanced technique is worthy for future research to better eliminate the source imprint and further improve the quality of FWI inverted velocity. Compared with the initial velocity (Fig. 2b), the FWI-inverted velocity (Fig. 6) recovers more detailed features and improves the resolution. We can also note that the improvement of the right part is minor due to the poor illumination caused by the sparse sources, which will be discussed later.

The GmRTM image using the FWI-inverted velocity model is shown in Fig. 7. It provides a better focusing and a reduced deviation between the focusing and the true source location (red dot in Fig. 7). The best focusing in Fig. 7 is found at the lateral location 1.99 km and depth 2.26 km, which effectively improves the prediction precision of the source location compared to the GmRTM result using the initial velocity model (Fig. 3).

In simultaneous inversion of passive source location and velocity model, the inversion result depends seriously on the initial velocity model. If the initial velocity is too far away from the true velocity, it is easy to fall into local minima in the simultaneous inversion. In the proposed method of this paper, we use a sequential method for passive source imaging and velocity inversion. Since the source location estimation is performed by finding the best focusing provided by high-resolution GmRTM, which is separate from the passive FWI. This could relax the dependency on the initial velocity model.

3.3 Influence of seismic noise on velocity inversion

The field microseismic data are generally noisy, which causes additional challenges for the source location estimation and velocity inversion. To evaluate the influence of seismic noise on passive FWI, we use Madagascar software to generate seismic random noise with broadband spectral, and add it to the noisy-free seismic recording (Fig. 4a). We use a pseudo-random algorithm for random noise generation, which is realized by setting an initial 'seed' for the random number generator. In our research, we use a nearly uniformly distributed sequence for random noise generation. In Fig. 8(a), we show the generated noisy recording with *S/N* (signal-to-noise ratio) = 20 dB (decibel). The inverted velocity model (Fig. 8b) after 50 iterations using this noisy recording contains some artifacts but recovers similar velocity features compared to the FWI-inverted velocity using the noise-free data (Fig. 6). In Fig. 8(c), we show the normalized misfit function versus iteration numbers using the noisy recording. Similar convergence rate is observed compared to the misfit function curve using noise-free recording (Fig. 5), but it is noted that there is relatively larger data residual due to the existence of random noise.

If we further increase the level of noise and generate much noisier recording with *S/N* = 5 dB (Fig. 9a) for inversion, the inverted model (Fig. 9b) can still recover most of the velocity features compared to the model using the noise-free data (Fig. 6), but much more artifacts are introduced, especially in the shallower part.

3.4 Influence of source distribution and density

The velocity structures and resolution of the FWI-inverted model (Fig. 6) in the right part are improved over the initial velocity model (Fig. 2b), but are not good enough due to insufficient illumination, as only one source located in the left part is used for inversion. A practical way to improve the illumination is to increase the number of passive-sources used. This is easy to achieve in field surveys; for example, we record numerous microseismic events during hydraulic fracturing.

We first increase the source number to three and still place them in the left part with lateral positions 1.20, 2.00 and 2.80 km. The receivers are still distributed sparsely, which are the same with our previous experiments. The FWI-inverted velocity model using these three sources are shown in Fig. 10, which provides higher resolution in the left part and clearer fault features in the middle part over the
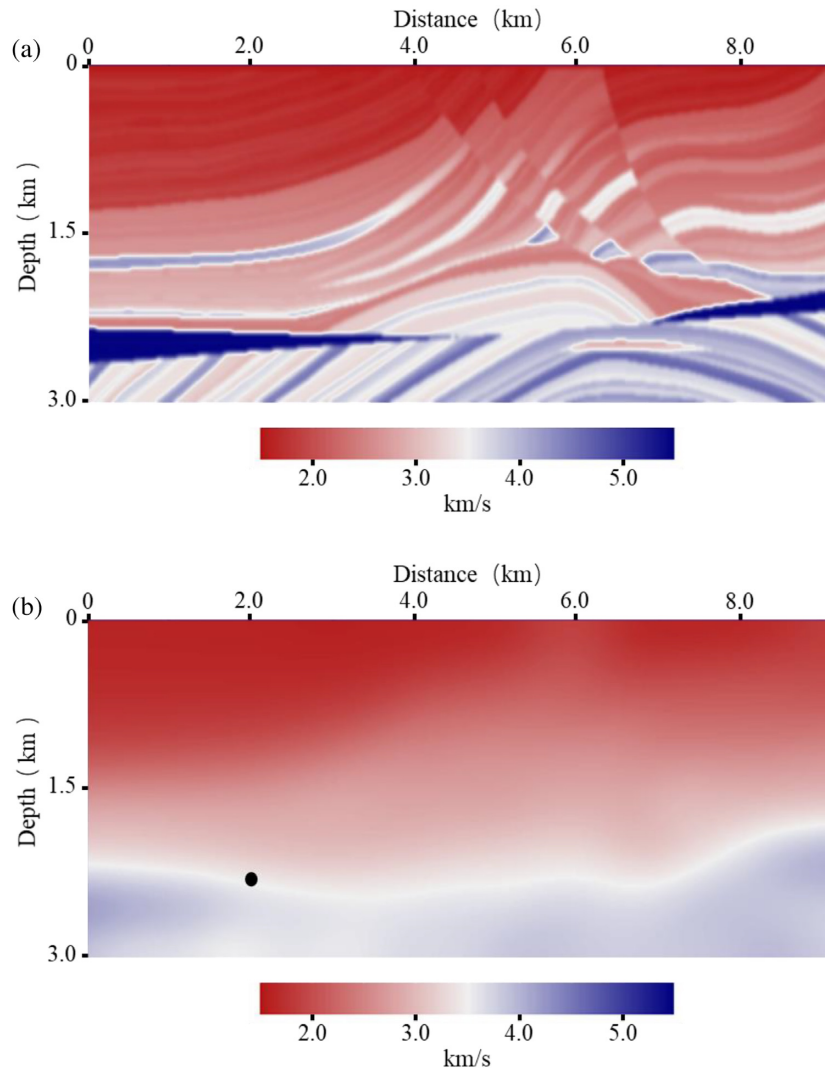
Figure 2. (a) True Marmousi velocity model. (b) Initial velocity model.
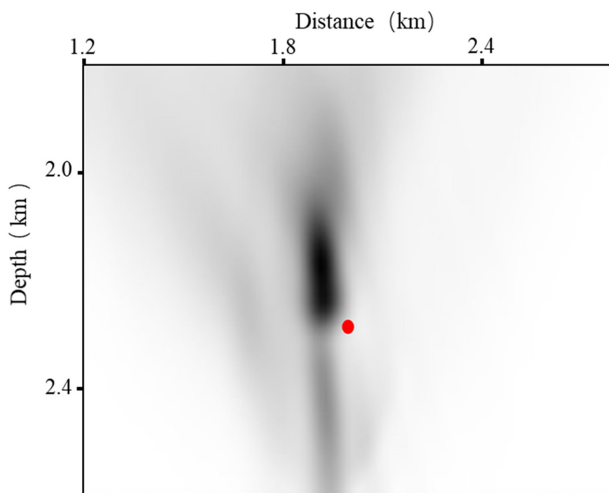
Figure 3. GmRTM result using the initial velocity model, behaving poor focusing and an obvious deviation between the focusing and the true source location (red dot).

inverted velocity model using only one source (Fig. 6). However, the improvement in the right part of the model is still not significant. Next, we still use three sources and sparse receivers for inversion, but place the sources more uniformly in the subsurface with lateral positions 2.00, 4.40 and 6.80 km. The FWI-inverted velocity model (Fig. 11) using these more uniformly distributed sources indicates higher resolution and reveals clearer features of the faults and the anticline in the middle and right part of the Marmousi model over the inverted result shown in Fig. 10. However, it is also noted that the inverted velocity model using more uniformly distributed sources (Fig. 11) behaves more artifacts and lower resolution in the left part over the one generated using three sources all located in the left part (Fig. 10).

We further use 15 uniformly distributed sources for inversion, which are located in the subsurface with starting lateral location 1.200 and 0.480 km interval. We use the same receiver distribution with the previous experiments. The FWI-inverted velocity model using 15 sources is shown in Fig. 12(a) (source locations indicated by black dots), which indicates an obvious improvement of the velocity precision over the results using fewer sources (Figs 6, 10 and 11). Especially, the FWI-inverted velocity model using 15
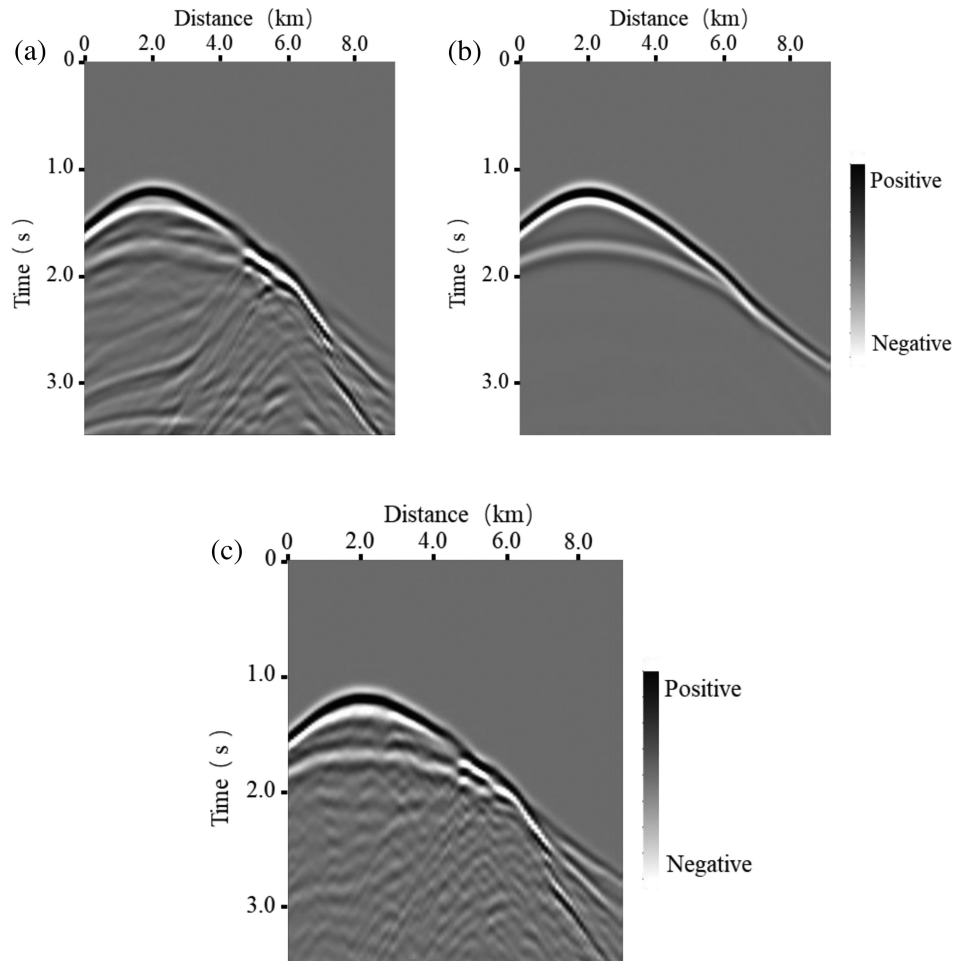
Figure 4. (a) Observed recording, (b) predicted recording using the initial velocity model and (c) predicted recording using the FWI-inverted velocity model.
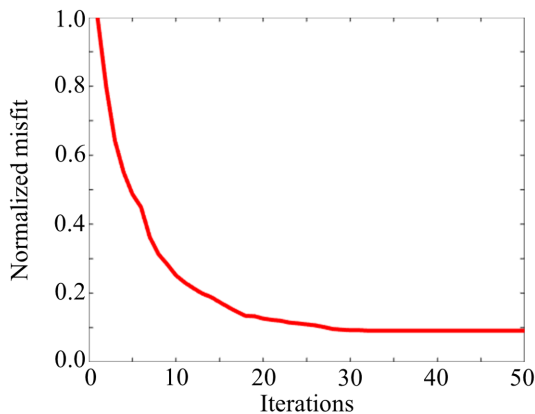
Figure 5. Normalized misfit function versus iteration numbers using single source.

sources (Fig. 12a) reveals more and clearer features of the entire Marmousi model, such as the faults, the anticline, and some other small-scale features, compared to the initial velocity model (Fig. 2b). Fig. 12(b) shows the normalized misfit function versus iteration numbers using 15 sources, indicating faster convergence rate compared to the result using single source (Fig. 5).

3.5 Influence of receiver density

We use sparse receivers with the same distribution for all the previous experiments. We also investigate the influence of the receiver density on the inversion, even though the dense receivers are not common in microseismic monitoring. The inversion is performed using 15 uniformly distributed sources at the same locations with the sources used in Fig. 12(a). However, the receiver space is reduced to 16 m. The FWI-inverted velocity model using 15 sources with dense receivers are shown in Fig. 13. It behaves higher resolution and reveals more small-scale features over the inverted velocity model using 15 sources with sparse receivers (Fig. 12a). It is also noted that the influence of source distribution and density play a more important role for inversion over the receiver density.

4 DISCUSSIONS

Since we estimate the source location and optimize the velocity model sequentially in the proposed method, the cross-talk limitation in the simultaneous FWI inversion could be partly relaxed. Especially, we use the high-resolution GmRTM to provide a better focusing, which helps to estimate the passive-source location more accurately. However, there is a demanding requirement of the
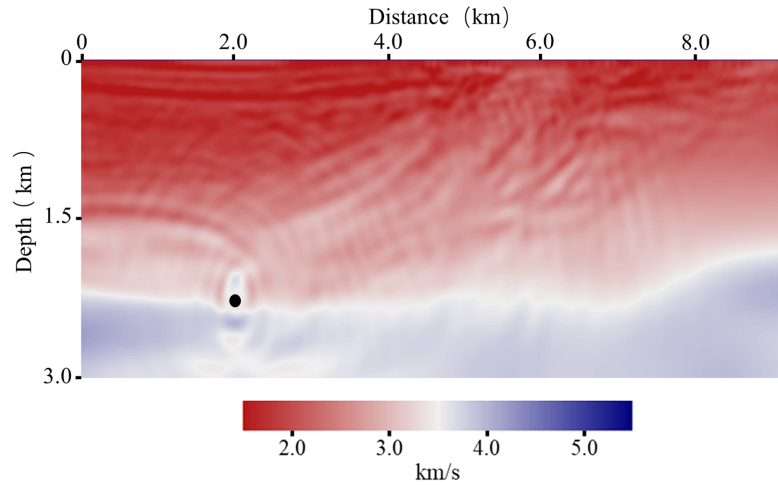
Figure 6. FWI-inverted velocity model using only one source located at lateral position 2.00 km and depth 2.27 km. Note that the FWI-inverted velocity recovers more detailed features and improves the resolution over the initial velocity model. It is also noted that the improvement of the right part is minor due to the poor illumination caused by the sparse sources.
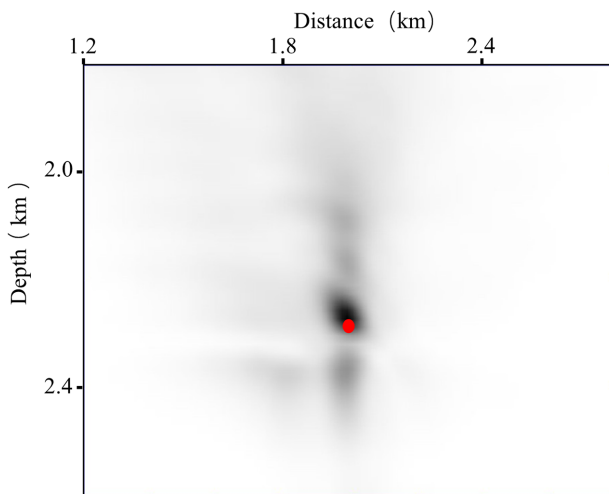
Figure 7. GmRTM recalculated using the FWI-inverted velocity model, providing a better focusing and a reduced deviation between the focusing and the true source location (red dot) compared to the GmRTM result using the initial velocity model (Fig. 3).

data storage and computation cost of this iterative passive-source estimation and velocity inversion approach.

Both the GmRTM used in passive-source estimation and passive-source FWI used in velocity inversion are time-consuming. For GmRTM, if we perform wavefield extrapolation independently for each receiver or receiver group, it could be computationally expensive. In our research, we first compute and storage the Green's function for each receiver, and then convolute between this Green's function and the recorded data in the image domain, similar to Nakata *et al.* (2016). This will increase the storage to some extent but will effectively reduce the computation cost. Other effective approaches to reduce the storage and computation cost in the proposed iterative passive-source estimation and velocity inversion method remains an interesting future research topic.

Cycle-skipping challenges both active-source and passive-source FWI. Several theory-based approaches are developed to relax the limitation of cycle-skipping problem in FWI, but most of the researches focus on the active-source, such as starting FWI with

super-low-frequency data (e.g. Wu *et al.* 2014; Li & Demanet 2016), separating the tomographic and migration components (e.g. Mora 1989; Alkhalifah 2015), or introducing additional dimensions to increase the convexity in waveform inversion (e.g. Sava & Fomel 2003; Biondi & Almomin 2014; Warner & Guasch 2014). For passive-source FWI, since we need to consider the influence of source-locations besides the velocity model, the cycle-skipping problem is more severe than active-source case. In the proposed method, we perform the source location estimation and velocity inversion in a sequential way. GmRTM provides an improved estimation of the source location with high-quality focusing, which helps relax the limitation of cycle-skipping in the simultaneous passive seismic inversion. However, further research is necessary to avoid the cycle-skipping problem in passive imaging and inversion more effectively. A potential solution is to bring the methods used in active-source FWI into passive-source FWI.

5 CONCLUSIONS

We have developed an iterative approach for passive-source estimation and velocity inversion based on full wave-equation methods. In each iteration, we first use the high-resolution GmRTM to estimate the source location. Then passive-source FWI is followed to update the velocity model using the estimated source locations by GmRTM. Passive source location estimation and velocity inversion are implemented sequentially. This iteration is indeed the key for the passive-seismic imaging with velocity estimation, because this iteration allows us to have better focusing of source locations compared to conventional wavefields scanning method, better sensitivity to structural velocities, and the fact that we do not need to rely on the initial source location for the inversion.

The numerical experiments on the Marmousi model indicate that the proposed iterative passive-source estimation and velocity inversion method could be adapted to complicated structures and noisy passive recordings. Increasing source density plays an important role to improve the imaging illumination and inversion quality. This passive-source estimation and velocity inversion is naturally extendable to 3-D data sets.
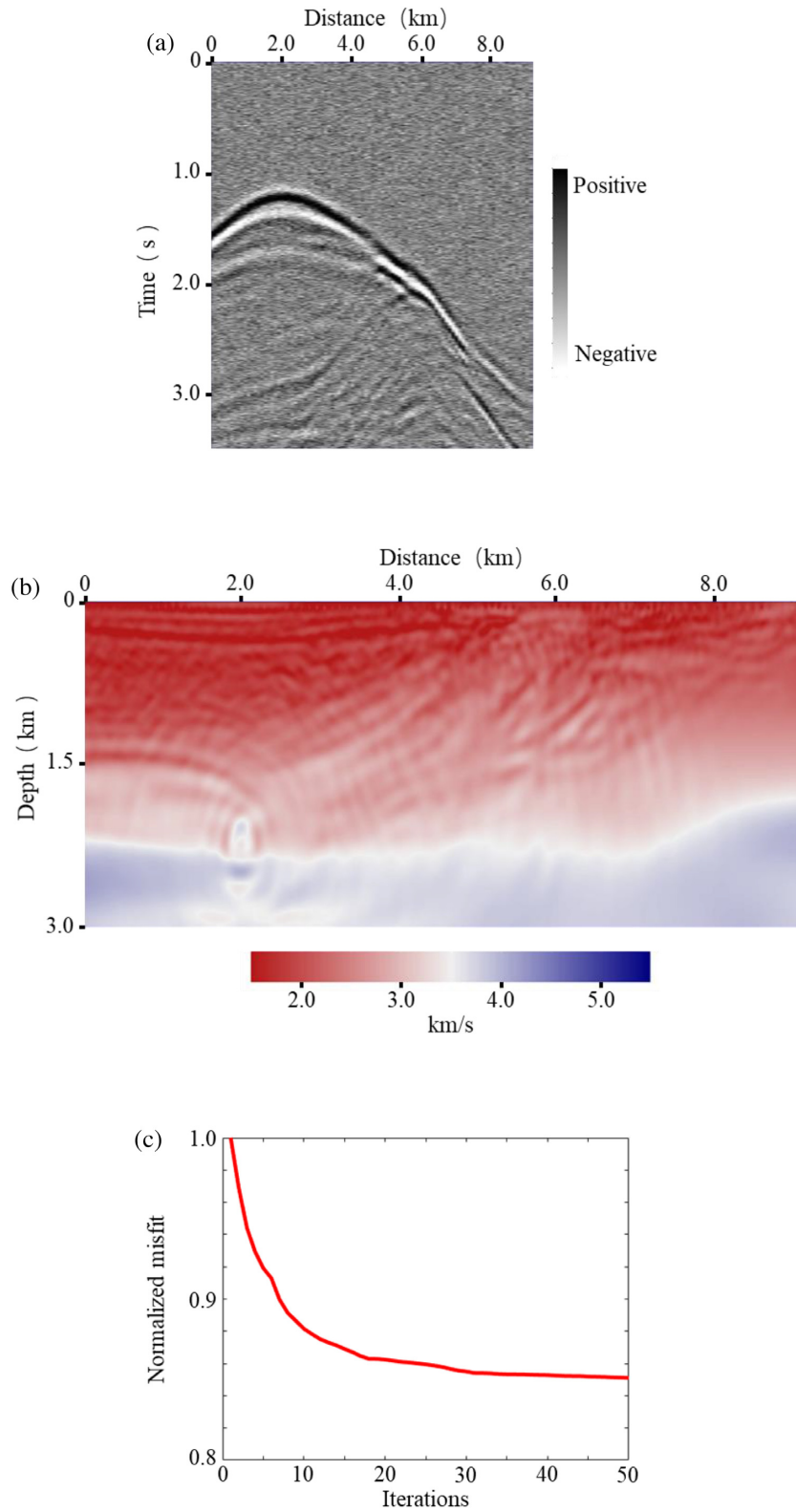
Figure 8. (a) Noisy passive-source recording with $S/N = 20$ dB, and (b) the corresponding FWI-inverted velocity model, behaving more artifacts but recovering similar velocity features compared to the FWI-inverted velocity using the noise-free data (Fig. 6). (c) Normalized misfit function versus iteration numbers using the noisy recording, showing similar convergence rate but relatively larger data residual compared to the result using noise-free recording (Fig. 5).
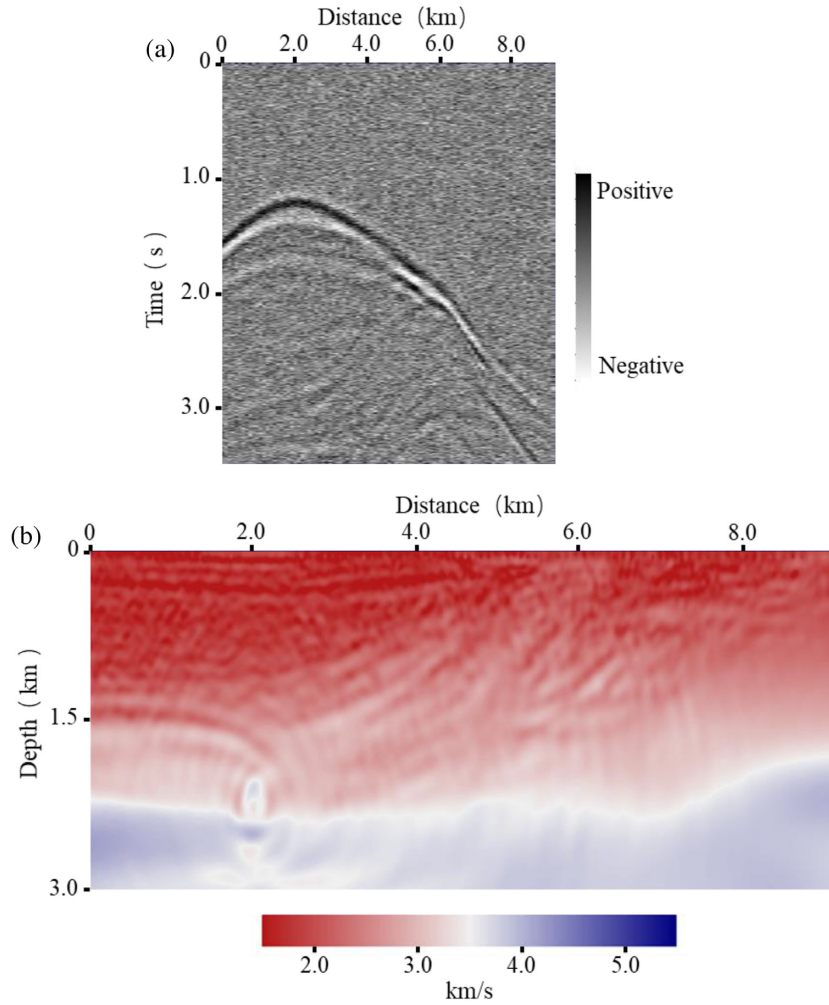
Figure 9. (a) Noisy passive-source recording with $S/N = 5$ dB, and (b) the corresponding FWI-inverted velocity model.
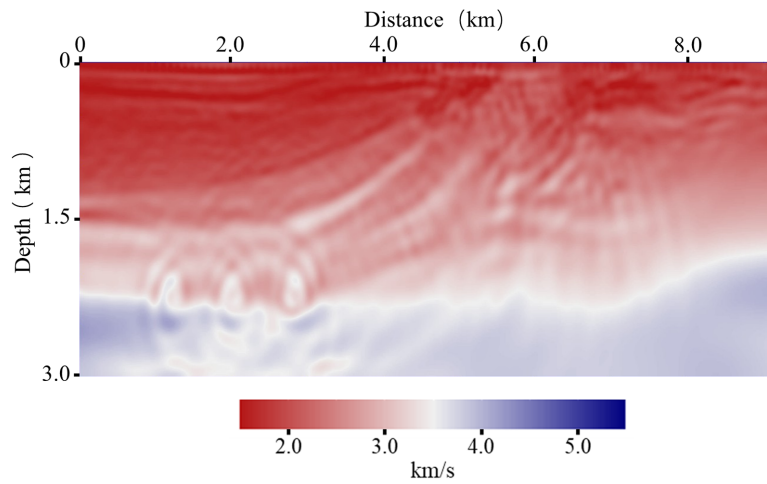
Figure 10. FWI-inverted velocity model using three sources located in the left part with lateral positions 1.200, 2.000 and 2.800 km. Note the higher resolution in the left part and clearer fault features in the middle part compared to the inverted velocity model using only one source (Fig. 6). However, the improvement in the right part of the model is still not significant.
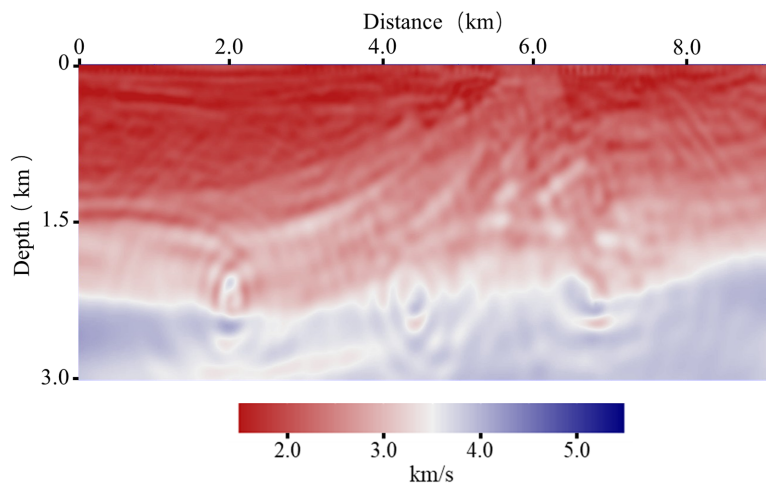
Figure 11. FWI-inverted velocity model using three more uniformly distributed sources with lateral positions 2.00, 4.40 and 6.80 km. Note the higher resolution and clearer features of the faults and the anticline in the middle and right part over the inverted velocity model shown in Fig. 10. However, it behaves more artifacts and lower resolution in the left part over the one generated using three sources all located in the left part (Fig. 10).
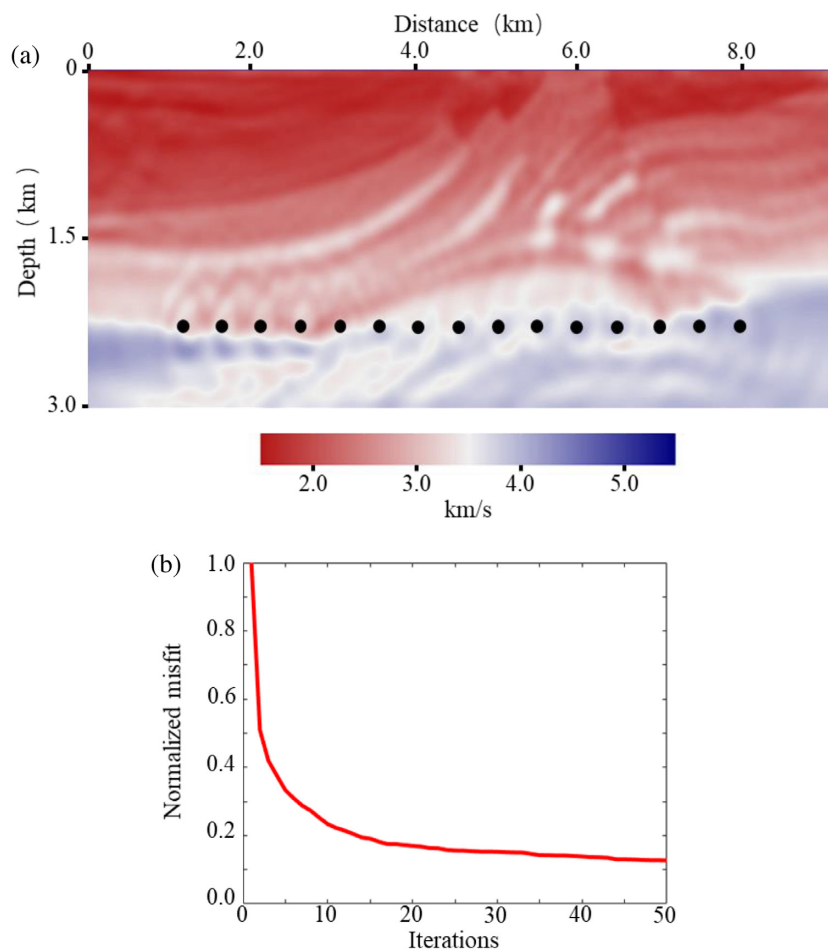
Figure 12. (a) FWI-inverted velocity model using 15 sources with sparse receivers, indicating an obvious improvement over the results using fewer sources and revealing much clearer features. (b) Normalized misfit function versus iteration numbers using 15 sources, indicating faster convergence rate compared to the result using single source (Fig. 5).
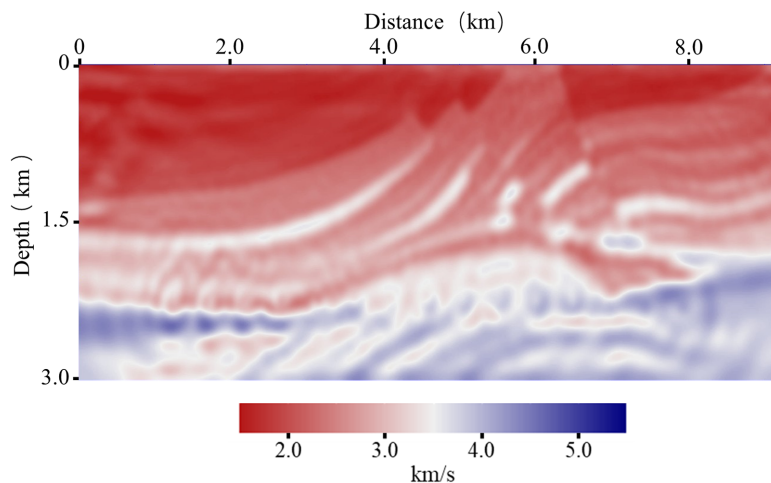
Figure 13. FWI-inverted velocity model using 15 sources with dense receivers, behaving higher resolution and revealing more small-scale features over the FWI-inverted model using 15 sources with sparse receivers (Fig. 12a).

ACKNOWLEDGEMENTS

REFERENCES

Aki, K., Christofferson, A. & Husebye, E.S., 1977. Determination of the three-dimensional seismic structure of the lithosphere, *J. geophys. Res.,* **82,** 277–296.

Alkhalifah, T., 2015. Scattering-angle based filtering of the waveform inversion gradients, *Geophys. J. Int.,* **200,** 363–373.

Artman, B., Podladtchikov, I. & Witten, B., 2010. Source location using time-reverse imaging, *Geophys. Prospect.,* **58,** 861–873.

Baysal, E., Kosloff, D.D. & Sherwood, J.W.C., 1983. Reverse-time migration, *Geophysics,* **48,** 1514–1524.

Biondi, B. & Almomin, A., 2014. Simultaneous inversion of full data bandwidth by tomographic full-waveform inversion, *Geophysics,* **79,** WA129–WA140.

Brossier, R., Operto, S. & Virieux, J., 2010. Which data residual norm for robust elastic frequency-domain full waveform inversion?, *Geophysics,* **75,** R37–R46.

Chang, W.F. & McMechan, G.A., 1986. Reverse-time migration of offset vertical seismic profiling data using the excitation-time imaging condition, *Geophysics,* **51,** 67–84.

Claerbout, J., 1971. Toward a unified theory of reflector mapping, *Geophysics,* **36,** 467–481.

Dohmen, T., Blangy, J.-P. & Zhang, J., 2014. Microseismic depletion delineation, *Interpretation,* **2,** SG1–SG13.

Dueker, K.G. & Sheehan, A.F., 1997. Mantle discontinuity structure from midpoint stacks of converted P to S waves across the Yellowstone hotspot track, *J. geophys. Res.,* **102,** 8313–8327.

Duncan, P.M. & Eisner, L., 2010. Reservoir characterization using surface microseismic monitoring, *Geophysics,* **75,** 75A139–75A146.

Fomel, S., Sava, P., Vlad, I., Liu, Y. & Bashkardin, V., 2013. Madagascar: open-source software project for multidimensional data analysis and reproducible computational experiments, *Journal of Open Research Software,* **1,** e8.

Gajewski, D. & Tessmer, E., 2005. Reverse modelling for seismic event characterization, *Geophys. J. Int.,* **163,** 276–284.

Igonin, N. & Innanen, K.A., 2018. Analysis of simultaneous velocity and source parameter updates in microseismic FWI, in *Proceedings of the 88th Annual International Meeting,* SEG, Expanded Abstracts, pp. 1033–1037.

Innanen, K.A., 2014. Seismic AVO and the inverse hessian in precritical reflection full waveform inversion, *Geophys. J. Int.,* **199,** 717–734.

Kaelin, B. & Guitton, A., 2006. Imaging condition for reverse time migration, in *Proceedings of the 76th Annual International Meeting,* SEG, Expanded Abstracts, pp. 2594–2598.

Kamei, R. & Lumley, D., 2014. Passive-seismic imaging and velocity inversion using full wavefield methods, in *Proceedings of the 84th Annual International Meeting,* SEG, Expanded Abstracts, pp. 2273–2277.

Kamei, R. & Lumley, D., 2017. Full waveform inversion of repeating seismic events to estimate time-lapse velocity changes, *Geophys. J. Int.,* **209,** 1239–1264.

Kao, H. & Shan, S.-J., 2004. The source-scanning algorithm: mapping the distribution of seismic sources in time and space, *Geophys. J. Int.,* **157,** 589–594.

Li, F., Qin, Y. & Song, W., 2019. Waveform inversion-assisted distributed reverse time migration for microseismic location, *IEEE J. Select. Top. Appl. Earth Observ. Rem. Sens.,* **12**(4), 1327–1332.

Li, F., Bai, T., Nakata, N., Lyu, B. & Song, W., 2020. Efficient seismic source localization using simplified Gaussian beam time reversal imaging, *IEEE Trans. Geosci. Remote Sens.,* **58**(6), 4472–4478.

Li, Y.E. & Demanet, L., 2016. Full-waveform inversion with extrapolated low-frequency data, *Geophysics,* **81,** R339–R348.

Lyu, B., Li, F. & Marfurt, K.J., 2017. High-resolution reverse time migration with squared excitation-amplitude imaging condition, in *Proceedings of the 87th Annual International Meeting,* SEG, Expanded Abstracts, pp. 4438–4442.

Lyu, B., Nakata, N. & Marfurt, K.J., 2018. A reverse-time migration workflow of passive source with joint imaging conditions, in *Proceedings of the 88th Annual International Meeting,* SEG, Expanded Abstracts, pp. 2947–2951.

Loewenthal, D. & Hu, L.Z., 1991. Two methods for computing the imaging condition for common-shot prestack migration, *Geophysics,* **56,** 378–381.

Maxwell, S., 2014. *Microseismic Imaging of Hydraulic Fracturing: Improved Engineering of Unconventional Reservoirs,* SEG.

McMechan, G.A., 1982. Determination of source parameters by wavefield extrapolation, *Geophys. J. R. astr. Soc.,* **71,** 613–628.

McMechan, G.A., 1983. Migration by extrapolation of time-dependent boundary values, *Geophys. Prospect.,* **31,** 413–420.

Mora, P.R., 1987. Nonlinear two-dimensional elastic inversion of multi-offset seismic data, *Geophysics,* **52,** 1211–1228.

Mora, P., 1989. *Inversion = Migration + Tomography,* Springer.

Nakata, N. & Beroza, G.C., 2015. Reverse-time migration for microseismic sources using the geometric mean as an imaging condition, in *Proceedings of the 85th Annual International Meeting,* SEG, Expanded Abstracts, pp. 2451–2455.

Nakata, N., Beroza, G.C., Sun, J. & Fomel, S., 2016. Migration-based passive-source imaging for continuous data, in *Proceedings of the 86th Annual International Meeting,* SEG, Expanded Abstracts, pp. 2607–2611.

Nakata, N. & Beroza, G.C., 2016. Reverse time migration for microseismic sources using the geometric mean as an imaging condition, *Geophysics,* **81**(2), KS51–KS60.

Nguyen, B.D. & McMechan, G.A., 2013. Excitation-amplitude imaging condition for prestack reverse-time migration, *Geophysics,* **78**, S37–S46.

Operto, S., Gholami, Y., Prieux, V., Ribodetti, A., Brossier, R., Metivier, L. & Virieux, J., 2013. A guided tour of multiparameter full-waveform inversion with multicomponent data: from theory to practice, *Leading Edge,* **32**, 1040–1054.

Pan, W., Innanen, K.A., Margrave, G.F., Fehler, M.C., Fang, X. & Li, J., 2016. Estimation of elastic constants for HTI media using Gauss-Newton and full-newton multiparameter full-waveform inversion, *Geophysics,* **81**, R275–R291.

Plessix, R.-E., 2006. A review of the adjoint-state method for computing the gradient of a functional with geophysical applications, *Geophys. J. Int.,* **167**, 495–503.

Pratt, R.G. & Chapman, C.H., 1992. Traveltime tomography in anisotropic media - II. Application, *Geophys. J. Int.,* **109**, 20–37.

Pratt, R.G., 1999. Seismic waveform inversion in the frequency domain, Part I: theory and verification in a physical scale model, *Geophysics,* **64**, 888–901.

Rietbrock, A. & Scherbaum, F., 1994. Acoustic imaging of earthquake sources from the Chalfant Valley, 1986, aftershock series, *Geophys. J. Int.,* **119**, 260–268.

Sava, P.C. & Fomel, S., 2003. Angle-domain common-image gathers by wavefield continuation methods, *Geophysics,* **68**, 1065–1074.

Shang, X., Hoop, M.V. & Hilst, R.D., 2012. Beyond receiver functions: passive source reverse time migration and inverse scattering of converted waves, *Geophys. Res. Lett.,* **39**, L15308.

Steiner, B., Saenger, E.H. & Schmalholz, S.M., 2008. Time reverse modeling of low-frequency microtremors: a potential method for hydrocarbon reservoir localization, *Geophys. Res. Lett.,* **35**, L03307.

Sun, J., Zhu, T., Fomel, S. & Song, W., 2015. Investigating the possibility of locating microseismic sources using distributed sensor networks, in *Proceedings of the 85th Annual International Meeting,* SEG, Expanded Abstracts, pp. 2485–2490.

Sun, J., Xue, Z., Zhu, T., Fomel, S. & Nakata, N., 2016. Full-waveform inversion of passive-seismic data for sources and velocities, in *Proceedings of the 86th Annual International Meeting,* SEG, Expanded Abstracts, pp. 1405–1410.

Tarantola, A., 1984. Inversion of seismic reflection data in the acoustic approximation, *Geophysics,* **49**, 1259–1266.

Tarantola, A., 1987. *Inverse Problem Theory: Methods for Data Fitting and Model Parameter Estimation,* Elsevier Science Publ. Co., Inc.

Virieux, J. & Operto, S., 2009. An overview of full-waveform inversion in exploration geophysics, *Geophysics,* **74**, WCC1–WCC26.

Waldhauser, F. & Ellsworth, W.L., 2000. A double-difference earthquake location algorithm: method and application to the Northern Hayward Fault, California, *Bull. seism. Soc. Am.,* **90**, 1353–1368.

Wang, Y., Dong, L., Liu, Y. & Yang, J., 2016. 2D frequency-domain elastic full-waveform inversion using the block-diagonal pseudo-Hessian approximation, *Geophysics,* **81**, R247–R259.

Wang, H. & Alkhalifah, T., 2018. Microseismic imaging using a source function independent full waveform inversion method, *Geophys. J. Int.,* **214**, 46–57.

Warner, M. *et al.*, 2013. Anisotropic 3D full-waveform inversion, *Geophysics,* **78**, R59–R80.

Warner, M. & Guasch, L., 2014. Adaptive waveform inversion: theory, in *Proceedings of the 84th Annual International Meeting,* SEG, Expanded Abstracts, pp. 1089–1093.

Wessels, S.A., De La Pena, A., Kratz, M., Williams-Stroud, S. & Jbeili, T., 2011. Identifying faults and fractures in unconventional reservoirs through microseismic monitoring, *First Break,* **29**, 99–104.

Witten, B. & Shragge, J., 2017. Microseismic image-domain velocity inversion: Marcellus Shale case study, *Geophysics,* **82**, KS99–KS112.

Whitmore, D.N., 1983. Iterative depth imaging by back time propagation, in *Proceedings of the 53rd Annual International Meeting,* SEG, Expanded Abstracts, pp. 382–386.

Williamson, P.R. & Worthington, M.H., 1993. Resolution limits in ray tomography due to wave behavior: numerical experiments, *Geophysics,* **58**, 727–735.

Wu, R.-S., Luo, J. & Wu, B., 2014. Seismic envelope inversion and modulation signal model, *Geophysics,* **79**, WA13–WA24.

Xu, S., Wang, D., Chen, F., Zhang, Y. & Lambare, G., 2012. Full waveform inversion for reflected seismic data, in *Proceedings of the 74th Annual International Conference and Exhibition,* EAGE, Extended Abstracts, pp. W024.

Yang, J. & Zhu, H., 2019. Locating and monitoring microseismicity, hydraulic fracture and earthquake rupture using elastic time-reversal imaging, *Geophys. J. Int.,* **216**, 1919–1937.

Zhu, H., Bozdağ, E. & Tromp, J., 2015. Seismic structure of the European upper mantle based on adjoint tomography, *Geophys. J. Int.,* **201**, 18–52.

Zhu, T., 2014. Time-reverse modelling of acoustic wave propagation in attenuating media, *Geophys. J. Int.,* **197**, 483–494.

APPENDIX: STRUCTURAL IMAGING USING PASSIVE-SOURCE RTM

Besides passive-source estimation and velocity inversion, we provide the structural imaging using passive-source data in Fig. 1. The passive-source RTM using multicomponent recorded data is performed by a zero-lag cross-correlation between the decoupled *P*- and *S*-wavefields (Shang *et al.* 2012). Only the receiver-side wavefields are used, which is different from the active-source case, which uses both the source- and receiver-side wavefields. Multicomponent seismic recordings are needed to perform the cross-correlation, but sometimes we only have vertical-component data. In our research, we adopt a similar idea borrowed from the active-source RTM (Baysal *et al.* 1983; McMechan 1983; Whitmore 1983), to implement the passive-source RTM, which only uses the vertical-component data.

With the estimated source location $\mathbf{x}_s$ and the inverted velocity model $v(\mathbf{x})$ from the iterative approach using GmRTM and passive-source FWI, we first generate the source-side *P*-wavefield u_{SP}, followed by the application of imaging conditions with the receiver-side back-propagated *P*-wavefield u_{RP}, to provide the structural imaging results. There are several different imaging conditions for RTM, such as amplitude-ratio (Claerbout 1971), zero-lag cross-correlation (Claerbout 1971), source-normalized cross-correlation (Claerbout 1971; Kaelin & Guitton 2006), excitation time (Chang & McMechan 1986; Loewenthal & Hu 1991), excitation amplitude (Nguyen & McMechan 2013) and squared excitation amplitude (Lyu *et al.* 2017, 2018).

In this paper, we implement the squared excitation-amplitude imaging condition on the passive-seismic data to provide structural images with high-resolution and fewer migration artifacts. The squared excitation-amplitude imaging condition is expressed as

$$I(\mathbf{x}) = \int_0^T \frac{|u_{RP}(\mathbf{x}, t)|\, u_{RP}(\mathbf{x}, t)\, \delta(\mathbf{x}, t_e)}{u_{SP\_max}(\mathbf{x}, t_e)\, u_{SP\_max}(\mathbf{x}, t_e)} dt \qquad (A1)$$

where t_e is the excitation time defined as the maximum source amplitude arrival time, and this amplitude is known as the excitation amplitude u_{SP_max}. δ represents the delta function of t_e. Eq. (A1) means that the imaging is only performed at the locations that satisfy the excitation-time. The squared excitation-amplitude imaging condition is actually performed non-linearly, but available to be used for structural imaging. We only need to save the excitation-time and
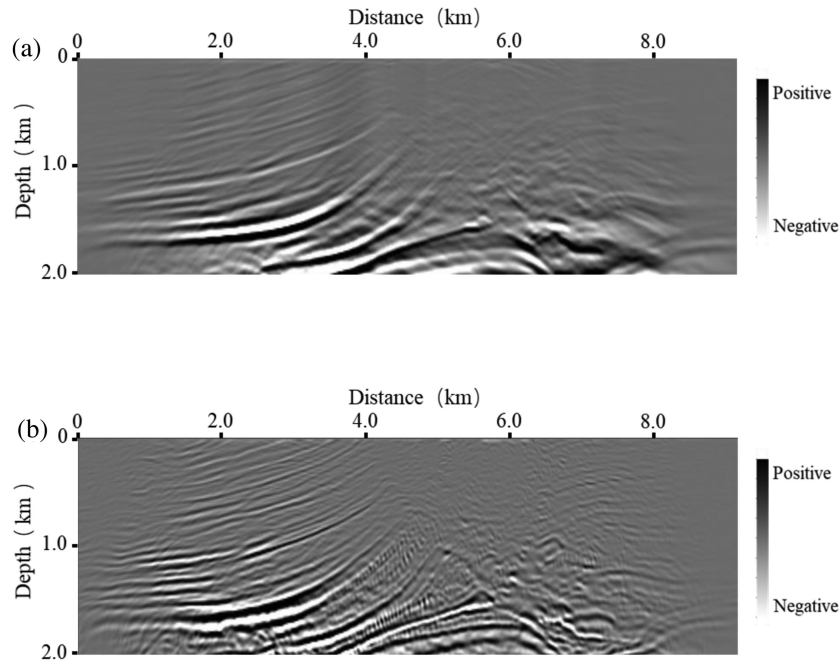
Figure A.1. Structural image by passive-source RTM with 15 sources using (a) the initial velocity model and (b) the FWI-inverted velocity model, providing higher resolution, better focusing, and clearer structures.

excitation-amplitude during wave propagation, which sidesteps the large storage requirement in the cross-correlation RTM. The imaging is only implemented at the locations that satisfy the excitation-time, which improves the resolution and reduces the migration artifacts.

Following Fig. 1, we provide the subsurface structural imaging using the passive-source RTM: we first perform the forward modeling of the source wavefields using the optimized source locations and velocity model, followed by an application of imaging condition with the back-propagated receiver wavefields. We use the high-resolution squared excitation-amplitude imaging condition for passive-source RTM. It faces the multipathing challenge in areas with complicated subsurface structures, as only the most energetic parts of the wavefields are used for imaging. For the left structures of the Marmousi model with relatively small dipping angles, we only need to save one amplitude arrival for imaging. However, it doesn't work in other areas with complicated structures, such as faults and steep reflectors. To deal with this multipathing issue, we save three amplitude arrivals for RTM imaging. It does not require additional wavefield extrapolation, but requires additional three times storage cost of excitation-time and excitation-amplitude. However, the storage cost of three amplitude arrivals is even much smaller than the one in cross-correlation method which saves all the extrapolated wavefields.

We then compute the structural imaging using 15 sources with sparse receivers and show the RTM images in Fig. A1. Compared with the RTM image using the initial velocity model (Fig. A1a), the RTM image using the FWI-inverted (Fig. A1b) provides higher resolution and better focusing. It is also noted that the faults, anticline and some other structures are better imaged in the RTM result using the FWI-inverted velocity model.